ELSEVIER

Contents lists available at ScienceDirect

Experimental Thermal and Fluid Science

journal homepage: www.elsevier.com/locate/etfs



Check for updates

Dynamics of ice melting by an immiscible liquid layer heated from above

Hamed Farmahini Farahani ^{a,*}, Tatsunori Hayashi ^b, Hirotaka Sakaue ^b, Ali S. Rangwala ^a

- ^a Department of Fire Protection Engineering, Worcester Polytechnic Institute, Worcester, MA 01609, USA
- b Department of Aerospace and Mechanical Engineering, University of Notre Dame, Notre Dame, IN 46556, USA

ARTICLE INFO

Keywords:
Melting
Immiscible layer
Convection
Interfacial flows
Meltflow film

ABSTRACT

A series of experiments were conducted to investigate the melting of ice adjacent to a water-immiscible liquid layer (n-dodecane) exposed to radiation from above. The experimental setup consisted of a borosilicate container containing an ice wall and a layer of n-dodecane heated from above. In addition to tracking the movement of the melt front, Particle Image Velocimetry (PIV) and Background Oriented Schlieren (BOS) measurements were conducted on the liquid-phase. Two distinct melting regimes were found to dominate the melting process. First was the uniform melting across the contact area with the immiscible liquid layer for low radiation levels (\sim 1 kW/m^2). Second was the lateral intrusion regime, where a depression near free surface of the liquid forms in ice and grows laterally for radiation level greater than $\sim 1 \ kW/m^2$. The ice surface remained flat and smooth in uniform melting regime, whereas in the lateral intrusion regime a series of rivulets were formed that carved valleys on the ice. PIV measurements showed a surface flow toward the ice for all heat flux levels caused by surface-tension forces. Increase of the heat flux levels caused a transition to multi-roll structure in the flow field. This multi-roll structure, which is accompanied by a recirculation zone near the ice, increased heat transfer near the surface of the liquid causing lateral intrusion regime, BOS measurements indicated presence of density gradients below the free surface of n-dodecane and in regions near the ice that are caused by local small-scale temperature gradients. The current experiments were conducted to explore the melting dynamics and to shed light on the processes that influence the ice melting. Implications of such mechanisms in a real-life scenario, i.e. oil spill in ice-infested waters, needs to be explored further by using more liquids and improved accuracy of the diagnostic techniques.

1. Introduction

The changing Arctic conditions because of oil and gas related activities increase the possibility of oil spills. Contamination by spilled oils and cleanup chemicals could have catastrophic effects on the environment and biodiversity of coastal areas of the Arctic [1–3]. Massive volumes of contaminants can spread in ice-infested waters and cover a large area as they can be transported further when there is significant ice coverage [4]. Apart from contamination problems, another threat that is posed by spill of petroleum products is their effect on melting of the ice sheets [5]. This is due to the fact that oil layers potentially absorb more solar energy and could transfer that energy to the ice different than water.

Partial thaw occurs naturally every year and ice sheets partially disintegrate through melt pool evolution process [6]. However, presence of oil layers can fundamentally alter ice-melting behavior. In particular, presence of oil in melt pools potentially changes the dynamics of melting

and the melt pond evolution itself [7]. This is done through the changes in energy absorption and redistribution by oil layers in ice. Two energy sources can contribute to such an oil-ice energy exchange: 1- absorption of solar radiation by oil layers, 2- cleanup efforts (i.e., use of *in situ* burning). The former is characterized by low heat flux input $(0-0.5 \, \text{kW/m}^2)$ and long durations [6]. The latter is high in energy flux $(10-100 \, \text{kW/m}^2)$ but much shorter in durations (i.e. hours). Studies have shown supremacy of *in situ* burning (ISB) in icy waters to other cleanup methods [8–10]. However, this method can substantially increase the energy budget of oil and ice systems.

Since hydrocarbon oils are immiscible in water, transfer of energy from oil to the ice occurs differently than energy transfer from the water to ice. This is because the melt layer does not mix in the ambient liquid. Due to the immiscibility of oil and water, melted water will not diffuse into the fuel layer and flows downward, keeping the oil layer atop. Additionally, interfacial forces between the two liquids and air can cause convective flows that are unique to oil-ice systems [11–13]. These flows

^{*} Corresponding author at: Department of Fire Protection Engineering, Worcester Polytechnic Institute, 100 Institute Road, Worcester, MA 01609, USA. E-mail address: ffarahani.hamed@gmail.com (H. Farmahini Farahani).

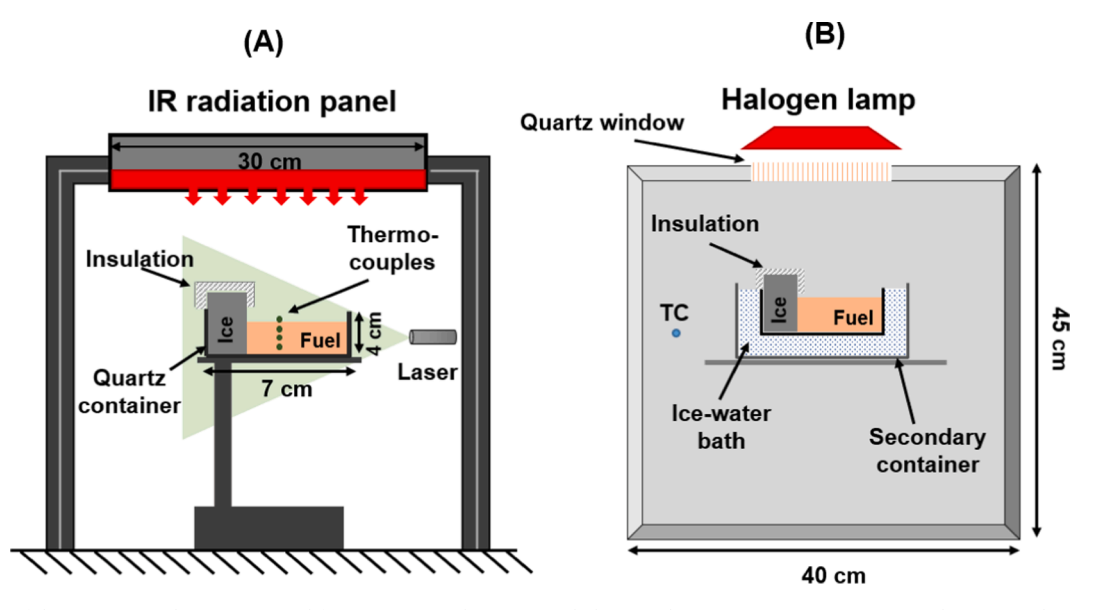


Fig. 1. Schematics of the experimental apparatus used for impinging radiation on n-dodecane adjacent to ice using (A) an IR radiation panel, (B) a 500 W halogen lamp with setup placed in a temperature control chamber.

are created due to the surface-tension effect caused by temperature gradient on the interface of fluids [14,15]. The ensuing flow patterns were previously found during flame spread over liquid fuels as a traveling wave at the top surface of the liquid fuels [16,17]. For a heated oil layer adjacent to ice, a strong surface flow toward the ice will be formed [12]. However, other details related to flow patterns in the liquid layer and the interaction of oil and melt-layer for different heating conditions are not studied yet. Therefore, it is necessary to understand the liquid-phase flow field in an immiscible layer to probe the heat transfer processes to the ice.

The focus of the current study is to scrutinize the transfer of energy into the liquid fuel layer and to the ice. This requires an understanding of the liquid state in terms of temperature and motion. To date only a few studies have been undertaken to address the oil-ice interaction and how it could enhance ice melting [11,12]. Melting of ice adjacent to immiscible liquid layers involves unique processes that are not well understood as explained above. Exploration of the controlling parameters of melting of ice because of the two energy inputs requires detailed experiments quantifying the melting behavior and the liquid flow field.

The objective of current study is to investigate the phenomenon of melting by immiscible liquids through exploratory experiments. Identifying the processes involved in this phenomenon is a first step to understand the important physics of melting by immiscible liquids. Such understanding will pave the way for more systematic studies, and also computational modeling on the subject to analyze the controlling parameters of melting. After such studies, it is possible to provide estimation or engineering applications related to this subject to deliver effective solutions for environmental protection. Such findings are also useful for storage energy systems that work with phase-change principles or latent heat energy storage [18].

2. Experiment description

2.1. Main setup

An experimental setup was developed to study different aspects of melting that is induced by an adjacent heated immiscible layer. The schematic of the experimental setup used in this study is shown in Fig. 1a-b. The main setup as depicted in Fig. 1-a consisted of a 30 by 30 cm square-shaped Infra-Red radiant panel (Omega Engineering, QC series, 4000 W-240 V) calibrated to an accuracy of 10% in the range of

 $2-30~kW/m^2$. Calibration was performed by a water-cooled heat flux gauge (Schmidt-Boelter type) for delivery of a relatively uniform heat flux to a target 9 cm below the panel bottom surface. IR radiation levels applied to the liquid in this study were 3.1, 6.6, and $11.0~kW/m^2$. Below the IR radiation panel, a custom-made square-shaped open top borosilicate container with side length of 7 cm and depth of 4 cm was used to hold the ice and the liquid fuel. Each experiment used an ice wall with approximate dimension of 7 $cm \times 4.5~cm \times 2~cm$ placed on the side of the container adjacent to $\sim 2.5~cm$ deep fuel layer. The top part of the ice wall was covered with an insulation shield during the experiments to prevent melting of the top section of the ice (the part above the liquid surface and exposed to air). The borosilicate container was immersed to the brim in a secondary container ($10~cm \times 10~cm \times 5~cm$) holding water and ice at 0 $^{\circ}C$ to isolate the outer walls of the inner container and create adiabatic wall condition.

Additional experiments with a 500 W Halogen lamp were performed to mimic visible light exposure similar to sunlight. The heat flux received at the surface of the liquid fuel for these tests was approximately $0.5-1 \ kW/m^2$. Accurate measurement of heat flux for this condition was not possible due to low intensity of the source and relatively high noise present in the heat flux gage readings. Although the actual heat flux for this case is lower than $1 \, kW/m^2$, a nominal value of $1 \, kW/m^2$ m^2 was used for this condition in reporting the results of the experiment. Due to low melting rate of ice at the lowest heating level $(0.5-1 \text{ kW/m}^2)$, the fuel and ice container were placed in a controlled-temperature chamber as an additional measure to reduce the effect of ambient on melting rate. The temperature control chamber had a glass door that facilitated photographing the ice melting process. The temperature of air inside the chamber was monitored with a K-type thermocouple. The chamber was kept at temperatures around 4 °C. However, due to long duration of the experiment (~30 min), the inside air temperature rose to around 15 °C at the end of the experiments. Fig. 1a-b shows the two setups with important details and dimensions labeled. The secondary container was used in all melting experiments to reduce the effect of ambient but is not depicted in Fig. 1a. Experiments for each heat flux level for repeated three times to ensure repeatability of the experiments. Melting front shapes were found to be qualitatively very similar for experiments at each heat flux level. The duration of experiments, determined by the melting rate of ice, were obtained after experiments and were compared. The standard deviation of ice melting rate was within 8% of the average values across all heat flux levels.

Table 1 Thermophysical properties of n-dodecane (values given at 20 °C and 101.3 kPa) obtained by Aspen HYSYS™.

	Water solubility (mg/L)	Density (kg/m³)	Thermal expansion coefficient (1/K)	Surface tension coefficient* (N/m.K)	Dynamic viscosity (kg/m·s)	Thermal diffusivity (m^2/s)
n-dodecane C ₁₂ H ₂₆	$5 imes 10^{-3}$	749	0.62×10^{-3}	-0.78×10^{-4}	1.43×10^{-3}	8.9×10^{-8}

^{*} Surface tension of n-dodecane is approximately 27 \times 10^{-3} N/m at 20 $^{\circ}\text{C}.$

Ice walls were made using directional freezing to minimize inclusions of bubbles. The liquid fuel used in this study was n-dodecane ($C_{12}H_{26}$), which is a transparent saturated straight-chain hydrocarbon representative of medium-weight components of crude oil. Table 1 represents few of the relevant physical properties of n-dodecane. Solubility of n-dodecane in water and saltwater is an important parameter to ensure immiscibility and is shown to be negligible.

Experiments initially scrutinized the melting behavior of ice adjacent to n-dodecane under radiative heating of the liquid by recording the melting front shape with a camera. A Canon 7D DSLR camera (accompanied by a 100 mm focal length lens) was placed approximately at a distance of 30 cm from the container and directly faced the side of the ice wall. The camera recorded the melting front shape at intervals of 10 sec. In-depth temperature change of the liquid phase was recorded with four fine gauge wire thermocouples (type E, 0.25 mm wire diameter) placed vertically with 5 mm spacing. This array of thermocouple was placed in the center of the tray, ~ 1 cm away from the ice wall. Diagnostic techniques were used to observe the flow field of the liquid and investigate the dynamics between the liquid fuel and melting ice. PIV (particle image velocimetry) method was used to study the flow field of the liquid fuel. In addition, BOS (Background Oriented Schlieren) technique was used to visualize the interfacial regions of the fuel, where interaction between different fluids were most probable to occur. Details of these two methods are provided in section 2.2. The experiments were initiated with heating of the IR panel to the desired temperature, which corresponded to a certain heat flux and then the tray containing the ice and liquid was placed at a fixed distance below the center of IR radiation

2.2. Diagnostics (PIV and BOS)

Particle Image Velocimetry (PIV) and Background Oriented Schlieren (BOS) experiments were conducted in the secondary container (dimension of $10~cm \times 10~cm \times 5~cm$) for improved optical accessibility and elimination of reflections. Subsequently, the size of the ice walls

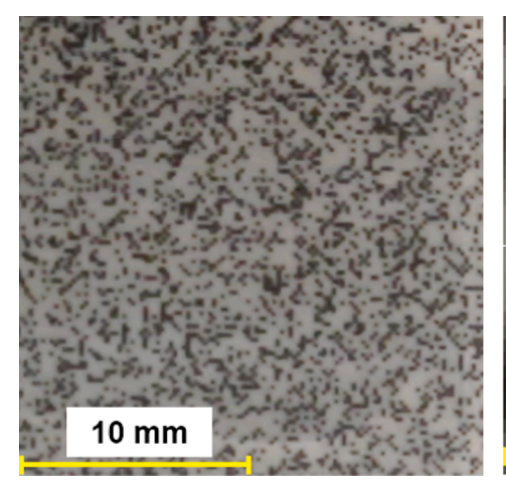
used for these experiments were scaled to size of the secondary container ($10~cm \times 5.5~cm \times 3~cm$). The velocity field on the mid-plane of the liquid fuel perpendicular to the ice wall was obtained by PIV measurements. A laser sheet was produced by placing a concave cylindrical lens on the path of a green diode laser with adjustable beam diameter. Seeding particles (glass spheres $10~\mu m$ diameter) were added to n-dodecane prior to pouring it into the borosilicate container. The particles specific gravity, relaxation time, and settling velocity for a liquid with density of $720~kg/m^3$ were calculated to be around 1.1, 0.11 μ s and 0.27 $\mu m/s$, respectively. The camera with recording rate of 30 fps was placed perpendicular and focused on the laser sheet that illuminated a slice of liquid fuel. The video files were processed to obtain individual frames in black and white and the PIV post-process was performed by PIVLab [19]. Cross correlation scheme with interrogation window size of 16 by 16 pixels was used for the post-process.

Background Oriented Schlieren technique was used to visualize the density gradients near the free surface of the liquid. BOS is a diagnostics technique mostly used in experimental aerodynamics research where supersonic flows are examined [20], but it can be used where density gradients are present. BOS technique employs a digital camera and a structured background to create sets of images to be processed with cross correlation algorithms, similar to PIV images postprocessing. The BOS method attains the first spatial derivative of the index of refraction. The index of refraction is then related to density by the Gladstone-Dale relation [21,22]. In the current experiments, a random generated dot pattern with dots of around 0.25 mm in diameter with variable number of dots were generated to attain optimal number of dots in each interrogation area. Fig. 2 shows the dot-generated background and its corresponding interrogation area.

3. Results

3.1. Melting by immiscible liquids

Melting requires energy to increase temperature of a solid to its



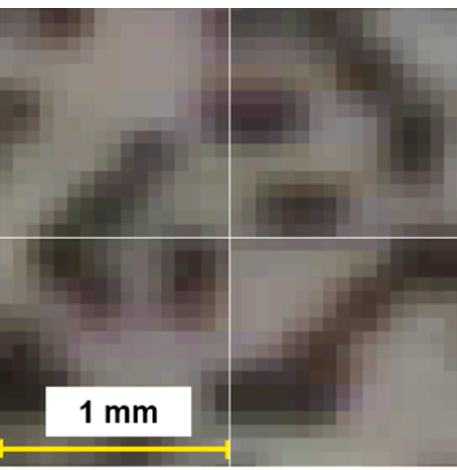


Fig. 2. Background of the random dot pattern used as imaged by the 1924×1080 pixels camera on a $10 \times 5cm$ field. Dots of diameter d = 0.25 mm were numerically generated, resulting in dots of approximately 4–5 pixels in the camera sensor. The magnification (b) represents 32×32 pixels, and 4 interrogation windows of size 16×16 pixels, used for the Digital Image Correlation, are shown for reference.

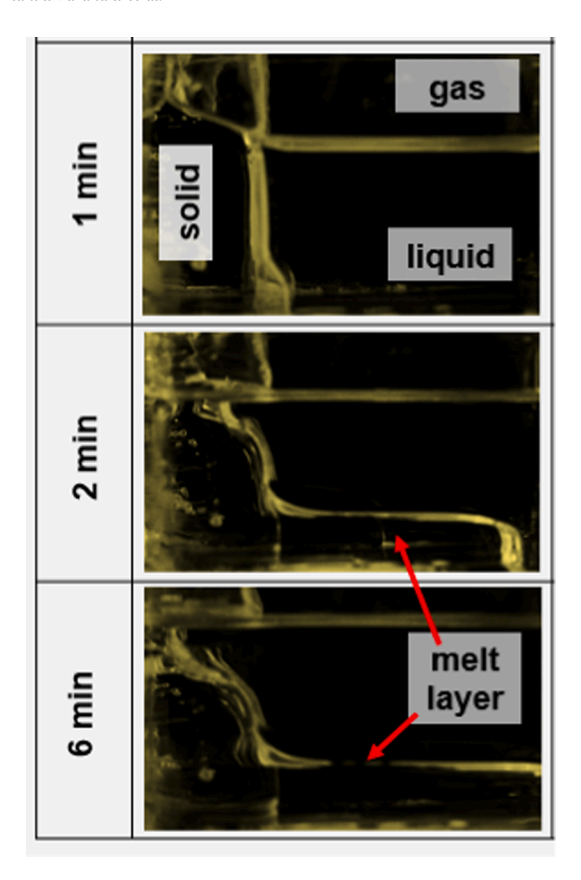


Fig. 3. Still photographs of ice melting by n-dodecane heated from above $(3.1 \, kW/m^2)$ and accumulation of meltwater below n-dodecane layer.

melting point and then more energy to change its phase, which makes melting an endothermic process. Melting is usually accompanied by diffusion of the melt layer into the ambient liquid. That is when the melt and ambient liquid are soluble. Hydrophobic liquids such as hydrocarbon fuels are immiscible in water and do not solve or diffuse in water. Consequently, melting of ice in an immiscible liquid (such as hydrocarbon fuels) occurs without mass diffusion, which means the two liquids form separate layers. Consequently, a melt film forms between the solid and ambient liquid when the immiscible liquid is in contact with the solid phase. Depending on the density difference between the two liquids, the melt film flows up or down along the interface of the two phases. When the density of the melt is higher than the immiscible liquid, the melt film flows down.

Fig. 3 shows the melting process captured by still photographs at different times during melting by an immiscible liquid layer at heating level of $3.1 \ kW/m^2$. Fig. 3 shows still photographs for a case where n-dodecane (density of $0.749 \ g/cm^3$) was heated from above and melted an adjacent ice wall causing the meltwater to flow down. This resulted in melting of the ice wall (lateral depression) and accumulation of meltwater below n-dodecane as seen in Fig. 3.

The geometry change of the ice during melting, i.e., lateral depression, is a function of both the immiscible liquid properties and the heating level [11]. The heating level has a more profound influence on the shape and amount of melting. Increase of the heating intensity for top heated immiscible liquid will naturally increase the melting rate due to the added energy to the overall thermal budget of the system. At low heating levels, melting rate will be small but the ice surface melts quite uniformly across its contact surface with the immiscible liquid (uniform melting regime). However, for the higher heat flux levels, the increase in melting rate manifests itself rather locally near free surface of the liquid (lateral intrusion regime).

Fig. 4 illustrates the two different melting front shapes, uniform and

lateral intrusion regime, from experiments with n-dodecane exposed to different radiation levels. The melting profiles (Fig. 4 a-c) are extracted from selected photographs that were taken during the experiments, while Fig. 4 d-f shows the photograph taken near the end of the corresponding experiment. Note that the end of each experiment is defined as the moment when liquid melts enough of the ice to reach the glass wall. The solid line markers indicate the liquid level for each time instant. Fig. 4a (uniform melting regime) shows a relative uniform melting front progression for heating level of 1 kW/m^2 from start (0 min) to near the end of an experiment (~22 min). Fig. 4b-c shows the lateral intrusion regime in the melting profile of the ice for heating level of 3.1 and 11 kW/m^2 . As can be seen the shape of the melting front near the end of this experiment is different and the lateral intrusion in ice is conspicuous.

The slope of the melting front (indicated with θ) can also be used to compare the melting progression. The melting front slope changed from a vertical line to nearly a horizontal one as shown in Fig. 4 d-f as indicated with θ . Another parameter that can be obtained from the cavity profiles are the melting intrusion velocity, which is calculated based on the initial thickness of the ice (~20 mm) divided by the duration of each experiment (i.e., the time it takes for the liquid to melt the ice and reach the glass wall). Melting intrusion velocity for 1, 3.1, 6.6 and $11.0 \, kW/m^2$ experiments were 0.8, 2.7, 4.3 and 5.2 mm/min, respectively. Note that the cavity profile resulted from experiments at 6.6 and $11 \, kW/m^2$ are qualitatively similar and therefore only the $11kW/m^2$ case is shown here. Solid horizontal line markers in Fig. 4 a-c mark the liquid free surface for each of the melting profiles.

Once the temperature of the ice is increased to its melting point the energy that is transferred to the ice will slowly melt the ice, which forms a thin film of melt flowing down the ice wall. The thickness of such layers were estimated to be around 250 to 800 μm reported in a previous study of melting by immiscible layers [23]. It is also stated the melt flow is a laminar unidirectional downward flow on the smooth surface of the ice. Estimation of the melt film thickness in this study suggests that larger thicknesses are expected. In addition, it is found that the flow of the melt film changes its dynamic causing change in morphology of the ice as the heating level passes a threshold value.

Fig. 5 a-b shows side and front view of an ice wall that was removed from an experiment with n-dodecane under 6.6 kW/m^2 incident heat flux. Fig. 5a shows the side view of the ice wall, after removal from the tray after about 4 min exposure time of the immiscible liquid to radiation. The yellow solid line and arrows in Fig. 5a illustrate the general path of melt flow. Although exact measurement of the melt film was not possible within the bounds of the current experimental setup, visual observations from a side view angle (using pixel conversion with a calibration target) yielded melt films with thicknesses of 700 to 1300 um. Note that the measurements of film thickness have large uncertainties. Regardless, such values are about twice the values reported previously [23], which are expected as the melting rates in the current experiments are generally higher. Additionally, the melt film is expected to flow down unidirectionally and thicken at lower part of the ice wall. However, at higher heating levels the melt film alters into running rivulets of meltwater. These rivulets cause formation of a series of vertical depressions on ice that assist the run-off of the meltwater.

Fig. 5b shows the front view of the same ice wall, depicting a series of vertical depressions carved in ice. These depressions appear when incident heat flux is higher than $\sim 1~kW/m^2$, which coincides with the onset of shift in melting shape of the ice, i.e., from uniform melting to lateral intrusion regime. The depressions become deeper (around 3 mm depth) as the heat flux to the surface of the liquid is increased (to accommodate the increased flow of meltwater). The blow-up section of Fig. 5b shows a qualitative velocity profile on the surface of ice that was recorded in PIV experiments and is illustrated here. Instead of a unidirectional flow, a narrow rapid stream of meltwater flowed down. Around this rivulet a slower reverse flow is induced that flowed upward. The thickness and form of the water run-off has implication for momentum exchange between the ice and the liquid that should be studied

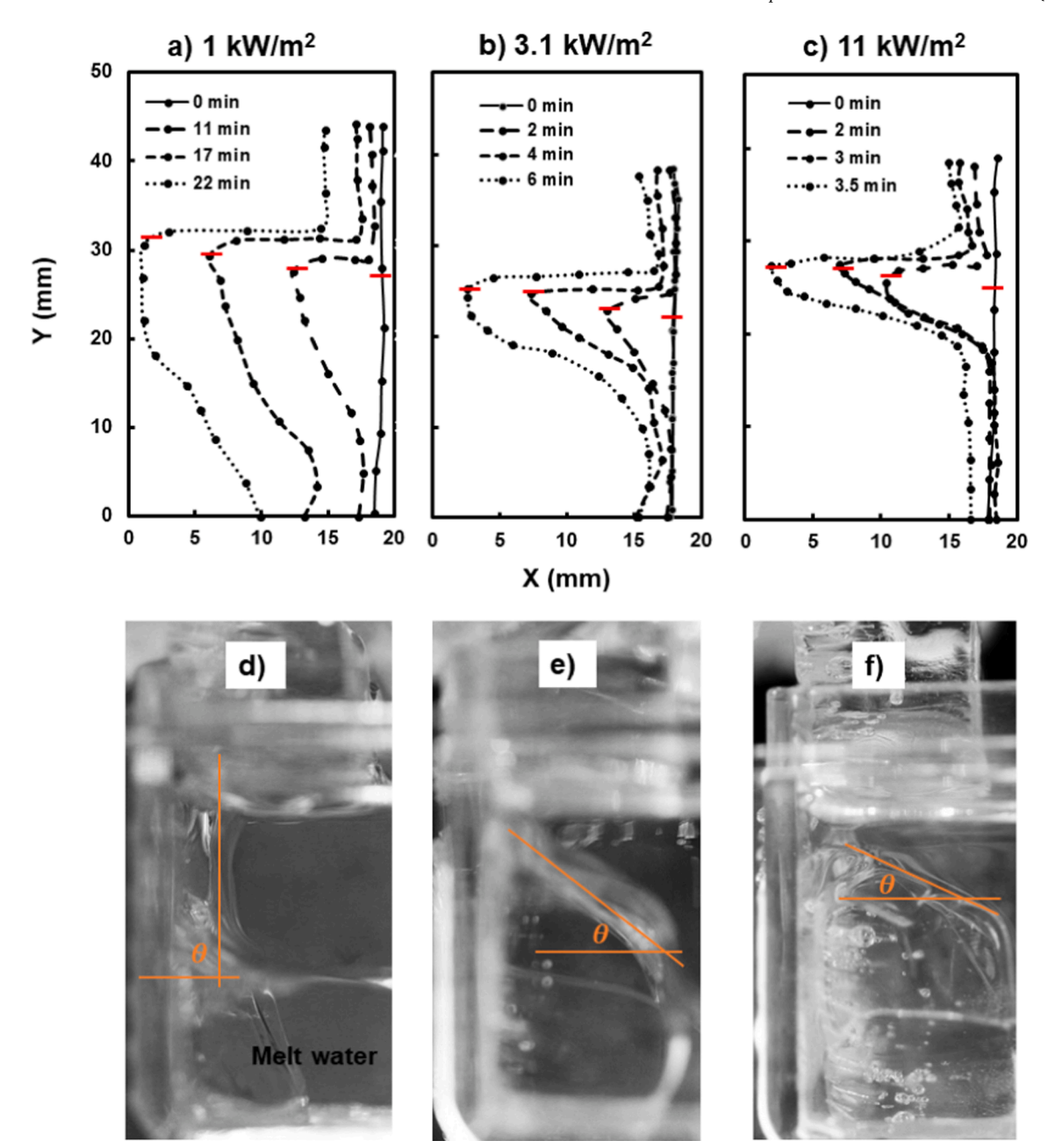


Fig. 4. Melting profile of ice adjacent to n-dodecane (a-c) and photographs taken near the end of each experiment (d-f) for 1, 3.1, and $11 \ kW/m^2$ radiation levels.

in more details in future studies.

As discussed through Fig. 4 and Fig. 5, immiscible layers heated from above could have two melting regimes based on the level of heat flux. The uniform melting regime at low heating levels transforms into lateral intrusion after a certain heat flux threshold, which melts the ice in the regions near the free surface of the liquid to create a lateral depression in ice. With further increase of the radiation output, this pocket becomes narrower. This geometry change in ice is studied in previous studies [24–28]. However, the details of mechanisms that led to this geometry change were not investigated. The following section describes the liquid-phase processes and scrutinizes the influence of these processes on melting.

3.2. Immiscible liquid processes

The heater panel emitted IR radiation down to the free surface of the liquid. The distance between the bottom surface of the emitter and top

surface of the liquid was large enough (9 cm) to eliminate any conduction or convection heat transfer from the heater to the liquid fuel surface. Therefore, only radiation was the heat transfer mechanism from heater to fuel surface. Straight-chain alkanes have four significant absorption band that can absorb up to 90% of IR radiation [29,30]. Given the depth of the liquid layer (25 mm), it can be assumed that the incident IR radiation is mostly absorbed by the liquid. This is not to say incident energy absorbed in its entirety. Subsequently, the liquid fuel used in the current experiments (n-dodecane, $C_{12}H_{26}$) absorbed a large portion of the incident radiation, which increased its temperature.

The temperature change of the liquid n-dodecane over the normalized time for three experiments at 1, 3.1, and $11 \ kw/m^2$ incident heat flux are presented in Fig. 6 a-c. Thermocouples were placed vertically with 5 mm intervals, where T4 indicates the thermocouple near the free surface and T1 is the thermocouple deepest in the liquid layer. All the experiments showed a vertical temperature gradient once a steady temperature was achieved. Naturally, this temperature gradient was

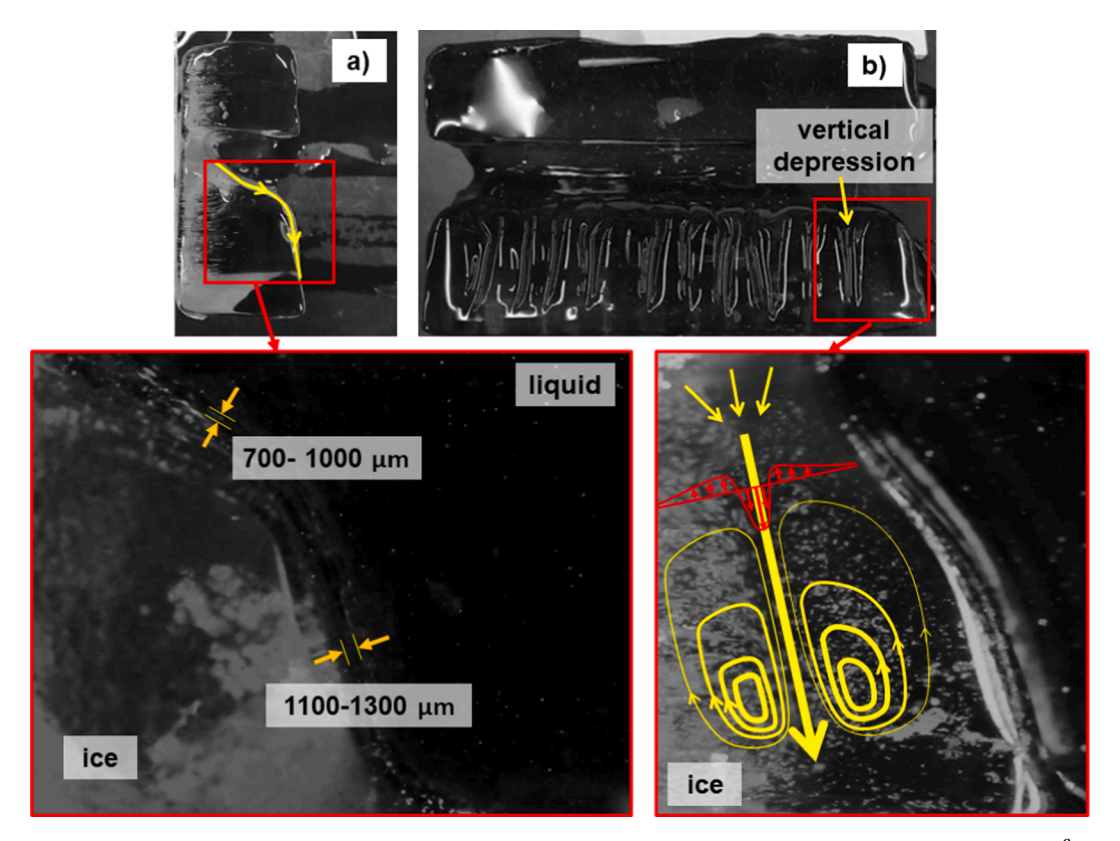


Fig. 5. a) Side and b) front view of the ice wall removed from container and photographed in experiment with heating level of $6.6kW/m^2$. Blow up images are recorded during the experiment.

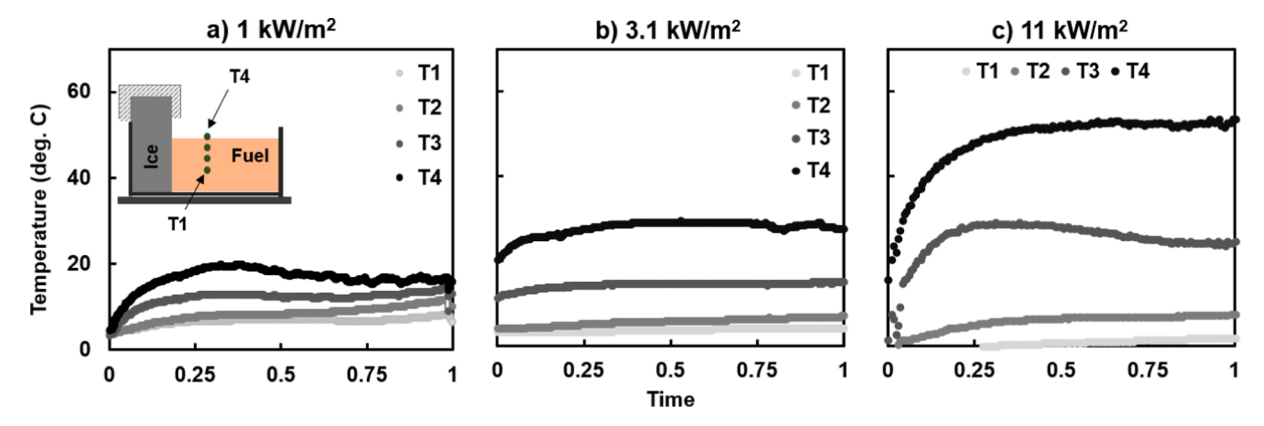


Fig. 6. Temperature history of n-dodecane recorded at the center of tray with four vertically placed thermocouples for experiments at (a) 1, (b) 3.1, and (c) $11 \, kW/m^2$.

larger for higher heat flux levels. Thermocouples closer to the free surface (T4) increased initially and then showed a steady value. Expectedly, the experiments at $11~kW/m^2$ showed a sharp increase in temperature reaching a maximum of $\sim 54~^{\circ}C$, while the temperature for experiments at 1 and $3.1~kW/m^2$ followed a smooth trend reaching a maximum of 22 and 31 $^{\circ}C$, respectively. For all incident heat fluxes, the main increase in temperature occurred at T4 and T3 locations, which correspond to a 5 mm thick layer below the free surface of liquids. This is where most of the incident radiation is absorbed. Note that the liquid surface moved up slightly during the experiments at $1~kW/m^2$, while the thermocouple was fixed. Therefore, the T4 thermocouple for this experiment shows slightly decreasing values since the TC bead was immersing gradually.

The temperature at a depth of around 15 mm (T1) increased minimally during the experiments for all experiments presented in Fig. 6. This means the radiation was mainly absorbed near the surface for all

experiments and the effect of in-depth radiation was limited. Additional experiments where the thermocouple tree was placed closer to the ice also showed very similar values, which means vertical gradient exist in the bulk of the liquid. Such temperature profiles are illustrated in a previous study [12] where a greater number of thermocouples were used. Note that T3 in $11\ kW/m^2$ experiment decreased after reaching a maximum, which is explained later. Temperature measurements along the depth of the liquids confirmed that most of the radiation is absorbed near the top surface at higher radiation levels.

It is not possible to identify the melting regime from the temperature histories of the three experiments presented in Fig. 6. As can be seen, the top layer temperature of the experiments at 1 and $3.1 \ kW/m^2$ have relatively low values but their melting shape is very different as was shown in Fig. 4. However, as the radiation increased, the temperature difference between T1 and T4 location became significant. This can be

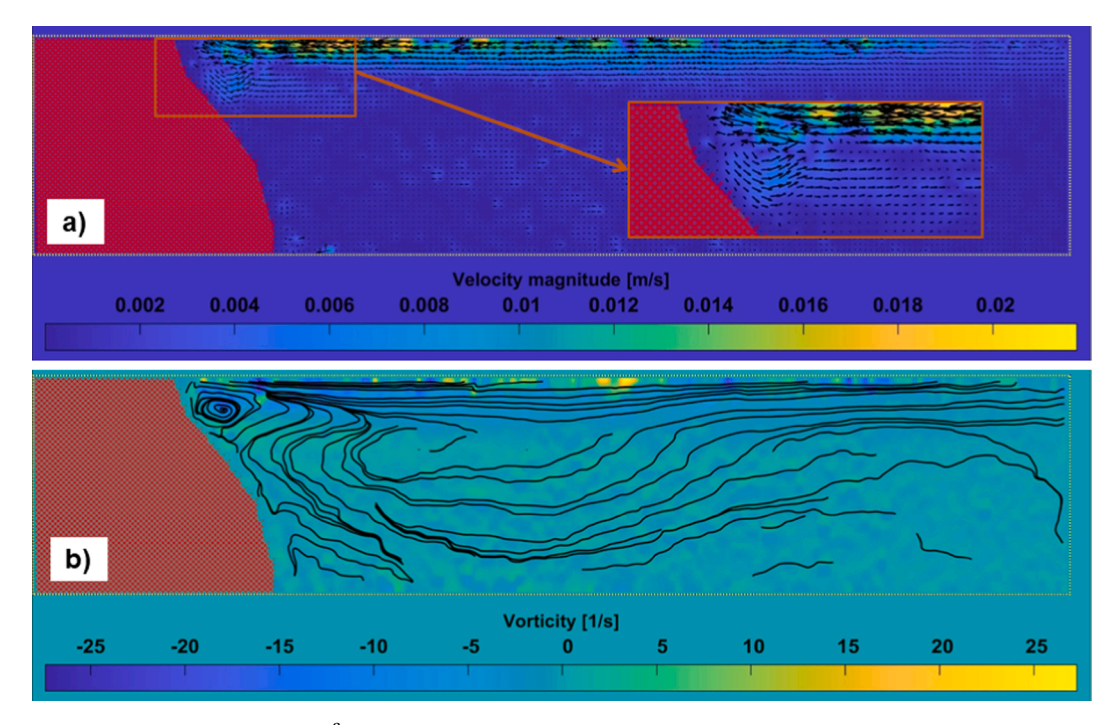


Fig. 7. Flow field of n-dodecane exposed to $1.5 \, kW/m^2$ showing the instantaneous (a) vector field with background color map of velocity magnitude (m/s) and (b) streamlines of flow with background color map of vorticity magnitude (1/s).

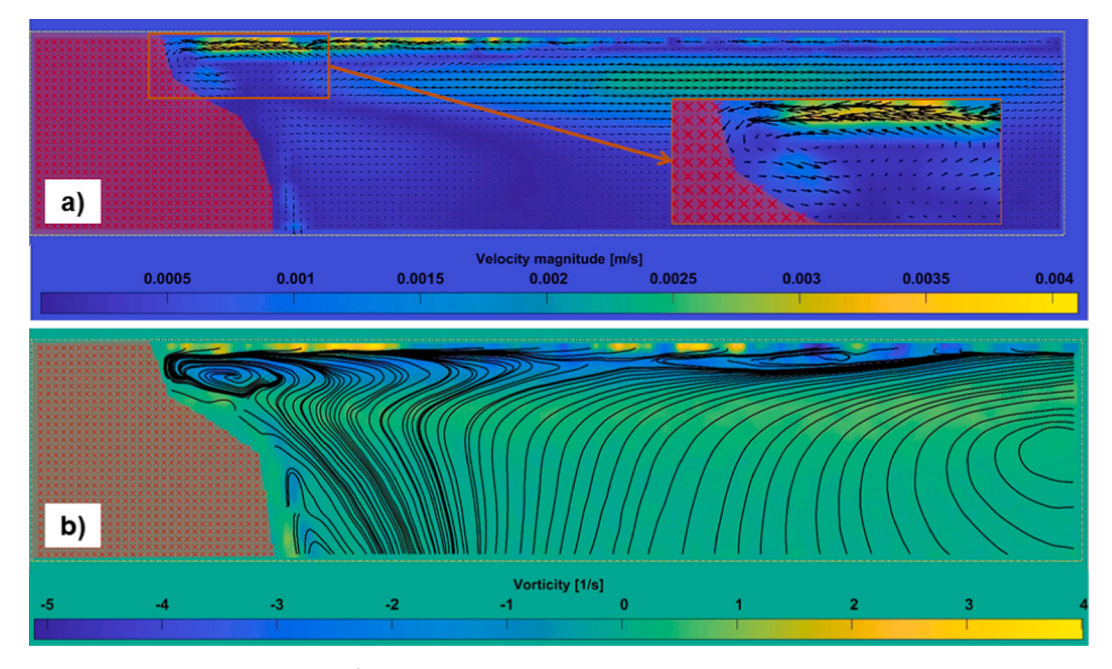


Fig. 8. Flow field of n-dodecane exposed to 6.6 kW/m^2 showing (a) averaged vector field with background color map of velocity magnitude (m/s) and (b) instantaneous streamlines of flow with background color map of vorticity magnitude (1/s) (b).

explained through the convective field in the liquid.

To study the convective field of the liquid phase, a series of PIV experiments were conducted as part of this study. The following describes PIV results of experiments with n-dodecane exposed to radiation intensity of 3.1, 6.6, and 11 kW/m^2 . Due to the use of the halogen lamp and the physical space limitations, obtaining PIV results for experiments at 1 kW/m^2 was not possible. PIV experiments were conducted in the secondary container for improved optical accessibility and elimination of reflections (dimension of $10\ cm \times 10\ cm \times 5\ cm$). Fig. 7a shows the instantaneous vector field of n-dodecane adjacent to an ice wall with the

background of velocity magnitude. Fig. 7b shows the streamlines of vorticity in the background of vorticity map. Ice is masked with color red on the left of each figure. The flow field throughout the duration of this experiment remained similar. Fluid flow is mostly observed below the free surface of the liquid. This surface flow is moving towards the ice wall with velocity of around 0.01 to 0.014 *m/s*. The arriving flow at the ice wall flows down, which forms a recirculating zone near ice as shown in Fig. 7b. The return flow is not discernable in the vector field, but the vorticity streamlines suggest return flow is mostly through the bulk of the liquid.

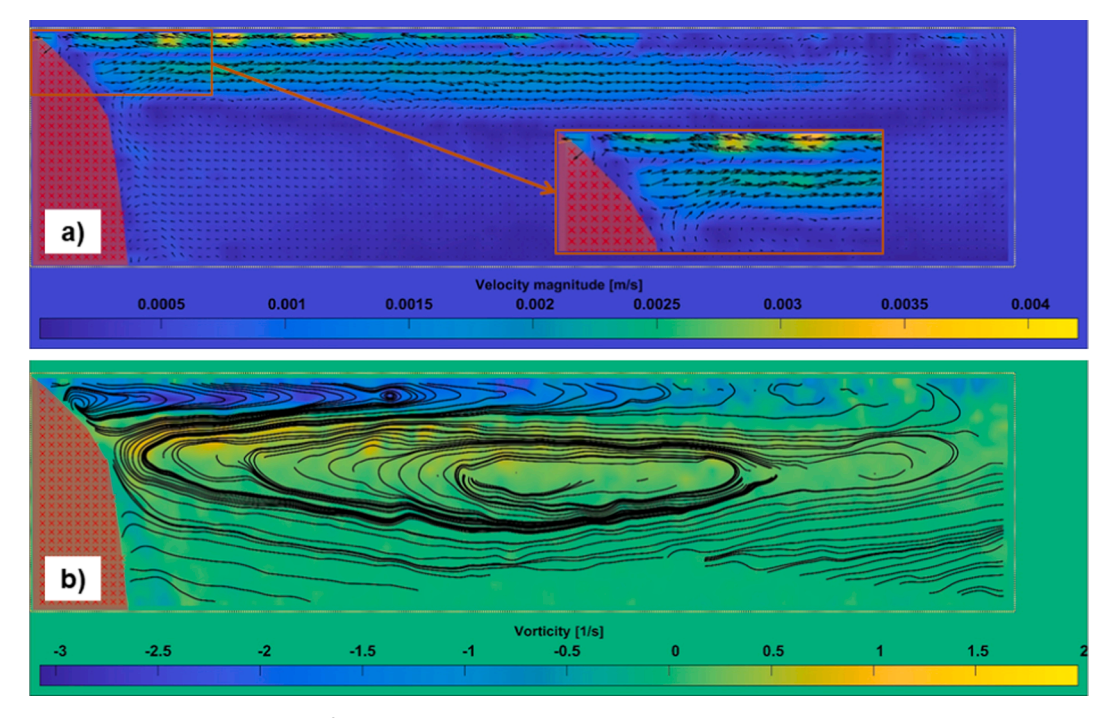


Fig. 9. Flow field of n-dodecane exposed to $11 \ kW/m^2$ showing (a) averaged vector field with background color map of velocity magnitude (m/s) and (b) instantaneous streamlines of flow with background color map of vorticity magnitude (1/s) (b).

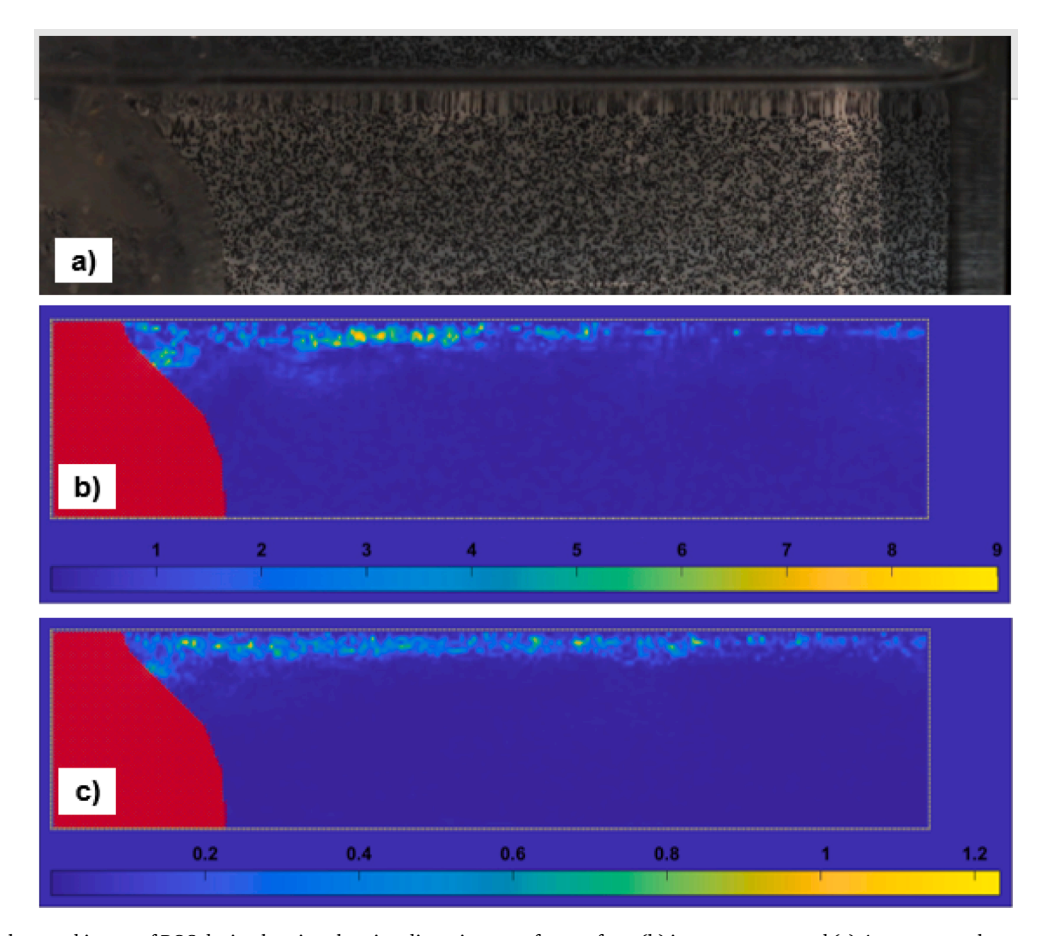


Fig. 10. (a) Raw background image of BOS during heating showing distortion near free surface, (b) instantaneous, and (c) 4 s average color map of color map of pixel displacement (pixel/frame) in n-dodecane.

Fig. 8a shows the vector field of n-dodecane exposed to 6.6 kW/m^2 radiation adjacent to an ice wall with the background of velocity magnitude. The vector field of Fig. 8a was averaged for 4 s due to optical distortions that eliminated a number of particles from the field of view. As the heating intensity was increased, the density gradients that were created in the liquid caused optical interferences that adversely affected PIV images. These interferences caused blockage and distortion of seeding particles scattered lights. Thus, portion of the signal was lost and obtaining the full image of vector field was not possible. Averaging in this situation provided an opportunity to see the general flow field, however, velocity magnitudes reported for the average results are significantly reduced. Nevertheless, increasing the radiation intensity to $6.6 \, kW/m^2$ caused the surface velocity to increase to around 0.014 to 0.018 m/s flowing towards the ice wall (measured by tracking single particles near surface). As fluid arrived at the wall, at a stagnation point, it was redirected by the recirculation zone near the wall. Fig. 8b shows the streamlines of vorticity in a background of vorticity map. As can be seen, the recirculation zone near the ice is pronounced and directed the flow down the ice. Return flow for this case was most discernible away from the ice and moving to the right-hand side (just below the surface flow). Although averaging gives an overall picture of the flow field, the instantaneous vorticity shows a number of circulating zones below the surface that are not apparent in Fig. 8b.

Increasing the radiation intensity further to 11 kW/m^2 changed the flow field both in terms of velocities and flow pattern of the liquid. However, due to difficulties with obtaining images of seeding particles most of the PIV signal was lost. Particle tracking showed velocities of more than 0.02 *m/s* near the surface towards the ice wall. Nonetheless, averaging the vector field and stacking them allows for observing the general trends of the flow. Fig. 9a shows the vector field of n-dodecane exposed to 11 kW/m^2 radiation adjacent to an ice wall with the background of velocity magnitude. In addition to the strong flow that is moving towards the ice below the free surface, there is a rather fast return flow just beneath it. This bottom flow extends from recirculation zone to almost the other end of the tray. The proximity of these two flows creates a large number of recirculation zones below the free surface that are observed in instantaneous streamlines but are not reported here. These rolls form a multi-roll flow structure below the surface. Fig. 9b shows the streamlines of vorticity in the background of vorticity map for the same experiment averaged for 4 s.

Particle tracking velocimetry near the free surface of n-dodecane revealed that liquid flow speed increased from 0.01 to 0.016 m/s and then to more than 0.02 m/s for 3.1, 6.6 and 11 kW/m^2 experiments, respectively. The significant increase of the velocity is directly related to the radiation intensities that induce surface-tension driven flows [27].

Density gradients that were created in the liquid introduced significant difficulties for PIV measurements, especially at higher radiation levels. These density gradients caused variation of refraction index, which leads to distortions of the view field. Using background Oriented Schlieren (BOS) allowed for measuring the distortion of optical field and finding the regions with density gradients, which points to steep temperature gradients in the liquid. Fig. 10a shows a raw image of a dotted background immersed in n-dodecane adjacent to an ice wall. Consecutive images taken from the background were processed using PIVLab [19] to find the displacement of pixels from one frame to another. Fig. 10b-c shows the instantaneous and averaged (4 s) color map of pixel displacement (pixel/frame) for n-dodecane exposed to $11 \ kW/m^2$ of radiation, respectively. The density gradients are mostly observed in the areas below the free surface and near the ice, which correspond to the areas of missing PIV signal and where most of the flow is observed.

4. Discussion

The energy balance at the interface of the solid–liquid, can be written with the following,.

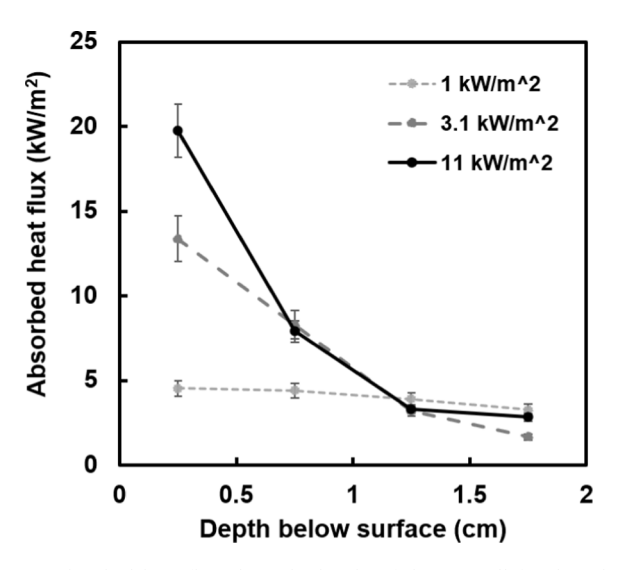


Fig. 11. Absorbed heat flux along the height of the ice wall for three heating conditions.

 Table 2

 Calculated Marangoni number at different heat flux levels.

Heat flux level (kW/m^2)	1	3.1	6.6	11
ΔT(°C) Ma (-)	$\begin{array}{c} 20 \\ 2.5 \times 10^6 \end{array}$	$\begin{array}{c} 30 \\ 3.7 \times 10^6 \end{array}$	$46 \\ 5.6 \times 10^6$	53 6.5×10^6

$$\dot{m}^{"}C_{p}(T_{m}-T_{ice})+\dot{m}^{"}L_{ice}=\dot{q}^{"}$$
. (1)

Here T_m, T_{ice} , and T_l are the melting point of the ice $(0^{\circ}C)$, initial temperature of the ice, and the liquid phase, respectively. C_p and L_{ice} are the specific heat and latent heat of melting of ice equal to 334 $(\frac{kJ}{k\sigma})$ and $2.1(\frac{kJ}{k\sigma K})$, respectively. Based on this equation, the energy flux received at the ice surface, $\dot{q}^{''}(\frac{kW}{m^2})$, contributes to increase the temperature of the ice (first term in Eq. 1) and to change its phase (second term in Eq. (2)). The first term can be neglected if ice temperature is assumed to be at melting point temperature [31]. Note that the ice used in the experiments were stored in a freezer at temperature of around -10 °C. If the temperature in the liquid across the ice surface is known then a local heat transfer coefficient could be calculated based on the local melting rate, $\dot{m}_{v}(\frac{kg}{m^{2}s})$, and temperature difference between liquid and ice, $(T_l - T_m)$. Without the knowledge of liquid temperature adjacent to the ice, the energy flux that contributed to melting of the ice along its height can be calculated using Eq. 1. Fig. 11 shows the absorbed energy flux along the height of the ice wall for different exposure conditions. Note that the local melting rates were obtained from Fig. 4 a-c. The regions where high absorption occurred corresponds to locations where the liquid experienced more convective motion as described in Section 3.2.

PIV measurements showed the horizontal flow of liquid toward the ice in a narrow layer (2–3 *mm*) below the top surface of n-dodecane for all the heat flux levels tested herein. This flow is created by interfacial instabilities due to gradient of surface-tension on the interface of n-dodecane and air [32]. Marangoni number can characterize the surface-tension force on the liquid–air interface. Marangoni number, *Ma*, for the current work is described with the following,.

$$Ma = \left(-\frac{\partial \sigma}{\partial T}\right) \frac{\Delta Td}{u\alpha} \tag{2}$$

where $\frac{\partial \sigma}{\partial t}$, d,μ , α are the coefficient of surface tension, characteristic length (assumed to be 2cm), dynamic viscosity and thermal diffusivity, respectively. The temperature difference between thermocouple location and ice surface, ΔT , is obtained from readings of T4 thermocouple,

Fig. 12. Schematics of flow in immiscible liquid showing (a) one roll structure, (b) transition to (c) multi-roll structure based on different heating intensities.

with the assumption of ice surface temperature of 0 °C. Table 2 presents the calculated Marangoni number for each experimental condition. Note that the values obtained are approximate as the liquid temperature used in estimation of temperature difference does not necessarily show the surface temperature. This is due to the slight rise in liquid level during experiments.

Based on the values shown in Table 2, the surface flow velocity can be expected to increase at higher heat flux levels. As such, the measured liquid velocity below the surface increased with increase in the radiation output. The arriving flow at a stagnation point near the ice is dissipated by a small recirculation zone that is formed near the ice wall. At low heating levels an overall counter clock-wise flow, one roll structure as shown in Fig. 12a, dominates the bulk of the liquid, which was observed in PIV studies of a previous study [12]. The recirculation zone in one-roll structure flow pattern only directs the arriving flow downward the ice. Therefore, the melting front shows uniform melting across its surface since the received energy from the top surface is evenly distributed on the ice surface.

Increasing the radiation level transforms the flow in two ways. First, the surface velocities increase as indicated by Marangoni number. At the same time, recirculation at the stagnation point of the flow redirects return flow into two distinguished paths; a horizontal return flow that appears below the surface moving to the right and away from the ice, and a downward flow near the ice wall (transition phase as shown in Fig. 12b). With further increase in the radiation level the surface-tension force becomes greater, thereby the horizontal return flow becomes much larger than the downward flow by the ice wall. As a result, multi-roll structure [33,34] appears below the surface of the liquid as shown in Fig. 12c. The horizontal return flow is formed to accommodate the increase in velocity of the surface flow. The two opposing horizontal flows below the surface of the liquid separate themselves from the bulk mixing that occurs in the liquid, and consequently preserve thermal energy in the top layer. Therefore, the lateral intrusion melting regime occurs due to the effects of multi-roll structure in the liquid layer. The momentum exchange of these two opposing flows also produces small eddies (as shown in Fig. 12c) that can be the cause for density gradients observed below the surface of n-dodecane. The strong return flow in multi-roll structure state could also explain why T3 thermocouple in the liquid (Fig. 6c) recorded decreasing values of temperature. Fig. 12 Provides schematic presentation for the different flow conditions described

The recirculation zone near the ice and overall flow pattern in the liquid elucidates the transition to lateral intrusion regime. Further increase of radiation output on the liquid surface creates the multi-roll flow condition and enhances the local melting, which makes the cavity narrower (reduce of θ). Other immiscible liquids will behave in the same manner, though the degree to which melting is enhanced depends on their surface-tension coefficient and viscosity [11]. Also, for a thinner layer of the immiscible liquid layer adjacent to ice, similar outcome is expected since the main mechanism for heat transfer to ice is confined to the very thin region below the free surface.

5. Conclusions

A series of experiments were conducted to investigate the melting of ice adjacent to an immiscible liquid layer exposed to radiation from above. Melting behavior of the ice along the fluid flow characteristics of the adjacent immiscible n-dodecane layer were obtained using PIV and BOS methods. Two distinct melting regimes of melting by n-dodecane were found to dominate the melting process. First is the uniform melting across the contact area with the immiscible liquid layer for low radiation levels ($\sim 1 \text{ kW/m}^2$). Second regime is the lateral intrusion, where a depression near free surface of the liquid forms in ice and grows laterally. The second regime is caused by higher radiation levels for ndodecane ($>1 \text{ kW/m}^2$). Meltwater flow also showed different characteristics in the two melting regimes, as evident from the melting face of the ice. The ice surface remained smooth in uniform melting regime, whereas in the lateral intrusion regime a series of rivulets were formed that carved valleys on the ice surface to accommodate the running stream of meltwater. The interaction of the two fluids for the latter case created a dynamic momentum exchange due to high flow of the meltwater down the ice surface. PIV measurements of convective flows in the immiscible liquid showed a constant surface flow toward the ice caused by surface-tension forces. These measurements disclosed a transition from one-roll structure when lateral intrusion melting regime was initiated. The weak recirculation zone that was created near the ice grew stronger as the radiation intensity was increased in lateral intrusion melting regime and created a rather strong return flow below the surface flow. The combination of the two opposing flows instigated separation of the top layer from the lower layer, which can maintain thermal exchange to the top layer and prevent mixing in the bulk of the liquid layer. BOS measurements indicated presence of density gradients below the free surface of n-dodecane and in regions near ice that are caused by local small-scale temperature gradients. It is speculated that these density gradients are produced by small eddies below the free surface due to interaction of the two opposing flows below the top surface of ndodecane.

The current experiments were conducted to explore the melting dynamics and to shed light on the processes that influence the ice melting. Multiple studies considering different aspects of this problem (melting rates, meltwater-liquid interaction, thermal and convective flow of the liquid) are needed to systematically address the dynamics discussed here. This first step of exploring the melting phenomenon by immiscible liquids shows the importance of attaining knowledge about the mechanisms involved. Implications of such mechanisms in a real-life scenario, i.e. oil spill in ice-infested waters, need to be explored further.

Declaration of Competing Interest

The authors declare that they have no known competing financial interests or personal relationships that could have appeared to influence the work reported in this paper.

Acknowledgement

This material is based upon work supported by the National Science Foundation under Grant No. 1938980. Any opinions, findings and conclusions or recommendations expressed in this material are those of the author(s) and do not necessarily reflect those of the National Science Foundation.

Appendix A. Supplementary data

Supplementary data to this article can be found online at https://doi.org/10.1016/j.expthermflusci.2022.110641.

References

- H. Blanken, L.B. Tremblay, S. Gaskin, A. Slavin, Modelling the long-term evolution of worst-case Arctic oil spills, Mar. Pollut. Bull. 116 (1–2) (2017) 315–331.
- [2] B.H. Hansen, D. Altin, K. Bonaunet, I.B. Øverjordet, Acute toxicity of eight oil spill response chemicals to temperate, boreal, and arctic species, Journal of Toxicology and Environmental Health, Part A 77 (9–11) (2014) 495–505.
- [3] M. Board, O.S. Board, N.R. Council, Responding to oil spills in the US Arctic marine environment, National Academies Press, 2014.
- [4] M. Fingas, B. Hollebone, Review of behaviour of oil in freezing environments, Mar. Pollut. Bull. 47 (9–12) (2003) 333–340.
- [5] R.O. Ramseier, Oil on Ice: How to Melt the Arctic and Warm the World, Environment: Science and Policy for Sustainable Development 16 (4) (1974) 6–14.
- [6] S. Zhang, J. Zhao, J. Shi, Y. Jiao, Surface heat budget and solar radiation allocation at a melt pond during summer in the central Arctic Ocean, Journal of Ocean University of China 13 (1) (2014) 45–50.
- [7] J. Freitag, H. Eicken, Meltwater circulation and permeability of Arctic summer sea ice derived from hydrological field experiments, J. Glaciol. 49 (166) (2003) 349–358.
- [8] V. Anghel, J. Armitage, F. Baig, K. Boniface, K. Boudjemline, J. Bueno, E. Charles, P.-L. Drouin, A. Erlandson, G. Gallant, R. Gazit, D. Godin, V.V. Golovko, C. Howard, R. Hydomako, C. Jewett, G. Jonkmans, Z. Liu, A. Robichaud, T. J. Stocki, M. Thompson, D. Waller, "A plastic scintillator-based muon tomography system with an integrated muon spectrometer," (in English), Nucl Instrum Meth A 798 (2015) 12–23.
- [9] J.L. Torero, S.M. Olenick, J.P. Garo, J.P. Vantelon, Determination of the burning characteristics of a slick of oil on water, Spill Sci. Technol. Bull. 8 (4) (2003) 379, 390
- [10] N. Wu, M. Baker, G. Kolb, J.L. Torero, Ignition, flame spread and mass burning characteristics of liquid fuels on a water bed, Spill Sci. Technol. Bull. 3 (4) (1996) 209–212.
- [11] H.F. Farahani, Y. Fu, G. Jomaas, A.S. Rangwala, Convection-driven cavity formation in ice adjacent to externally heated flammable and non-flammable liquids, Cold Reg. Sci. Technol. 154 (2018) 54–62.
- [12] H.F. Farahani, W.U.R. Alva, A.S. Rangwala, G. Jomaas, Convection-driven melting in an n-octane pool fire bounded by an ice wall, Combust. Flame 179 (2017) 219–227

- [13] K. Boniewicz-Szmyt, S.J. Pogorzelski, Influence of Surfactant Concentration and Temperature Gradients on Spreading of Crude-oil at Sea, Front. Mar. Sci. 5 (2018) 388
- [14] J.B. Keller, M.J. Miksis, Surface tension driven flows, SIAM J. Appl. Math. 43 (2) (1983) 268–277.
- [15] H. Saleh, N. Arbin, R. Roslan, I. Hashim, Visualization and analysis of surface tension and cooling effects on differentially heated cavity using heatline concept, Int. J. Heat Mass Transf. 55 (21–22) (2012) 6000–6009.
- [16] C. dl Blasi, On the role of surface-tension-driven flows in the uniform, near-flash flame spread over liquids, Combust. Sci. Technol. 110 (1) (1995) 555–561.
- [17] M. Li, S. Lu, R. Chen, J. Guo, C. Wang, Experimental investigation on flame spread over diesel fuel near sea level and at high altitude, Fuel 184 (2016) 665–671.
- [18] W.B. Ye, H.J. Guo, S.M. Huang, Y.X. Hong, Research on melting and solidification processes for enhanced double tubes with constant wall temperature/wall heat flux, Heat Transfer—Asian Research 47 (3) (2018) 583–599.
- [19] W. Thielicke, E.J. Stamhuis, PIVlab Towards User-friendly, Affordable and Accurate Digital Particle Image Velocimetry in MATLAB, Journal of Open Research Software 2 (2014), https://doi.org/10.5334/jors.bl.
- [20] M. Raffel, Background-oriented schlieren (BOS) techniques, Exp Fluids 56 (3)
- [21] E. Goldhahn, J. Seume, The background oriented schlieren technique: sensitivity, accuracy, resolution and application to a three-dimensional density field, Exp. Fluids 43 (2) (2007) 241–249.
- [22] L. Venkatakrishnan, G.E.A. Meier, Density measurements using the Background Oriented Schlieren technique, Exp. Fluids 37 (2) (2004) 237–247, https://doi.org/ 10.1007/s00348-004-0807-1.
- [23] M. Yamada, S. Fukusako, M.-E.-B. Sayed, Experiments on melting of a vertical ice layer immersed in immiscible liquid, Heat Mass Transf. 32 (6) (1997) 447–454.
- [24] P.W. Bellino, A.S. Rangwala, M.R. Flynn, A study of in situ burning of crude oil in an ice channel, Proc. Combust. Inst. 34 (2) (2013) 2539–2546, https://doi.org/ 10.1016/j.proci.2012.06.161.
- [25] H. Farmahini Farahani, X. Shi, A. Simeoni, A.S. Rangwala, A study on burning of crude oil in ice cavities, Proc. Combust. Inst. 35 (3) (2014) 2699–2706.
- [26] H. Farmahini Farahani, G. Jomaas, A.S. Rangwala, Effects of convective motion in n-octane pool fires in an ice cavity, Combust. Flame 162 (12) (2015) 4643–4648.
- [27] H. Farmahini Farahani, J. Torero, A.S. Rangwala, G. Jomaas, Scaling analysis of ice melting during burning of oil in ice-infested waters, Int. J. of Heat and Mass Transfer 130 (2019) 386–392.
- [28] X. Shi, P. Bellino, A. Simeoni, A. Rangwala, Experimental study of burning behavior of large-scale crude oil fires in ice cavities, Fire Saf. J. 79 (2016) 91–99.
- [29] A. Tuntomo, C. Tien, S. Park, Optical constants of liquid hydrocarbon fuels, Combust. Sci. Technol. 84 (1–6) (1992) 133–140.
- [30] J.M. Porter, J.B. Jeffries, R.K. Hanson, Mid-infrared absorption measurements of liquid hydrocarbon fuels near 3.4 μm, J. Quant. Spectrosc. Radiat. Transfer 110 (18) (2009) 2135–2147.
- [31] M. Yamada, S. Fukusako, and M. Eman-Bellah Sayed, "Melting heat transfer of a horizontal ice cylinder immersed within an immiscible liquid," 1996.
- [32] K. Smith, On convective instability induced by surface-tension gradients, J. Fluid Mech. 24 (2) (1966) 401–414.
- [33] D. Schwabe, A. Cramer, J. Schneider, S. Benz, J. Metzger, Experiments on the multi-roll-structure of thermocapillary flow in side-heated thin liquid layers, Adv. Space Res. 24 (10) (1999) 1367–1373.
- [34] B.-C. Sim, A. Zebib, D. Schwabe, Oscillatory thermocapillary convection in open cylindrical annuli. Part 2. Simulations, J. Fluid Mech. 491 (2003) 259.